An X-ray absorption near-edge structure (XANES) study of the Sn L3 edge in zirconium alloy oxide films formed during autoclave corrosion

Helen Hulme [a,c,*], Felicity Baxter [a], R. Prasath Babu [a], Melissa A. Denecke [b], Mhairi Gass [c], Axel Steuwer [d], Katarina Norén [e], Stefan Carlson [e], Michael Preuss [a]

[a] Materials Performance Centre, School of Materials, The University of Manchester, Manchester M13 9PL, UK
[b] The University of Manchester, Dalton Nuclear Institute & School of Chemistry, Manchester M13 9PL, UK
[c] Amec Foster Wheeler Clean Energy Europe, Walton House, Birchwood, WA3 6GA, UK
[d] Nelson Mandela Metropolitain University, Gardham Avenue, 6031 Port Elizabeth, South Africa
[e] MAX II Laboratory, Lund University, Ole Römers väg 1, 223 63 Lund, Sweden

ARTICLE INFO

ABSTRACT

Application of Sn L_3-XANES to study the oxidation state of alloying additions of tin (1–1.2 wt%) in <2 μm oxide layers formed on nuclear grade zirconium alloy has been demonstrated. Data obtained for metallic and corroded ZIRLO™ (1 wt% Sn) and Zircaloy-4 (1.2 wt% Sn) indicate tin has a similar chemical speciation in both metal alloys but this differs in the oxidised surface layers. By recording XANES at various incident angles to vary the photon penetration depth and amount of the oxide layer probed in the measurement, the authors found evidence that the oxidation of tin progresses with increasing oxide thickness.

1. Introduction

Zirconium alloys have been used as fuel-cladding material in water-cooled reactors for over 50 years. Favourable properties of zirconium in a nuclear core environment include low neutron absorption, good mechanical properties and high corrosion resistance under typical plant operating conditions; however, corrosion performance is a factor that can limit the life of Zr-based fuel assemblies. Despite decades of efforts, the corrosion mechanism for zirconium and its alloys is still not well understood, which makes prediction of long-life cladding behaviour challenging and means that any future alloy development can only be done on an empirical basis. Therefore, there are strong economic drivers for developing

a physically based understanding of the aqueous corrosion process of nuclear grade zirconium alloys.

Aqueous corrosion kinetics of zirconium alloys at high temperature and pressure initially follow a parabolic to cubic growth law, which eventually reaches a transition [1]. At transition, the protective state of the oxide breaks down and the corrosion kinetics first accelerate but subsequently slow down in a manner similar to the first cycle [1]. Such cyclic corrosion kinetics continue until linear breakaway growth is observed [2]. The corrosion rate and time at which transition occurs depends on a number of variables, including temperature, alloy composition, material processing history, corrosive environment and irradiation conditions [3–7].

During the initial rapid growth period of the pre-transition corrosion, small, equiaxed grains form at the metal/oxide interface, which have often been reported to have a high proportion of tetragonal oxide phase, stabilized by the small grain size [8–11]. As corrosion proceeds, the metal/oxide interface moves inwards and the corrosion rate reduces, which is associated with an epitaxial-type growth of oxide grains at the metal/oxide interface. It is still not entirely clear which phase of the oxide forms predominantly at this stage, but recent detailed grain mapping experiments have shown very high fractions of twin grain boundaries in the columnar oxide grains suggesting that most of the oxide at the metal/oxide interface

started out as tetragonal phase [12]. A number of diffraction studies have also shown that the compressive stresses in the oxide and the tetragonal phase fraction are highest at the metal/oxide interface, while further away from it the oxide stresses relax and the tetragonal phase fraction stabilizes at a comparatively low value [7,13,14]. This suggests that, in addition to the grain size stabilized tetragonal grains, stress stabilized tetragonal phase is present near the metal/oxide interface [7,11,13]. Interestingly, alloys that contain a higher tetragonal phase fraction close to the metal/oxide interface are associated with accelerated corrosion kinetics [7,15]. It should be noted that all these observations are related to out-of-pile investigations, i.e. autoclave-tested samples and not in-reactor tested material.

A number of hypotheses have been proposed to explain the cyclic behaviour of the corrosion kinetics. These hypotheses focus on changes to the thickness of a barrier oxide layer and factors impacting its protective nature, such as formation of cracks and increased porosity in the oxide or changes in the tetragonal phase fraction [5,16–18].

Alloying additions in the cladding are known to strongly influence its corrosion and hydrogen pick-up properties [19–21]. In particular, tin is known to have a detrimental effect on the corrosion behaviour of zirconium [22–24]; however, tin is added to some zirconium alloys, such as Zircaloy-4 and ZIRLO^{TM}, due to its favourable material strengthening properties [22]. Other alloying additions to Zircaloy-4, such as iron and chromium, have low solubility and are commonly found as second phase precipitates (SPPs) within the metal. In contrast, typical levels of tin additions in nuclear grade zirconium alloys do not exceed the solubility limit in zirconium and consequently tin is distributed uniformly throughout the zirconium metal matrix in form of a substitutional solid solution strengthening element. On oxidation of the metal, tin is then also incorporated in the oxide in a similar form [7,25]. Due to this high solubility, tin has not been studied as extensively as other alloying elements, which are distributed more heterogeneously.

Detailed characterisation of the stress state and tetragonal phase fraction using high-energy synchrotron X-ray diffraction [7] on Zr–Nb–Sn–Fe type alloys containing different levels of tin established a strong correlation between tin content and metastable tetragonal phase fraction. It was also shown that high initial levels of metastable tetragonal phase fractions result in increased levels of tetragonal to monoclinic phase transformation as corrosion proceeds causing significant damage in the oxide film in the form of cracking. The link between tin additions and tetragonal phase fraction is not immediately obvious. Apart from stress stabilisation and grain size, it is the number of oxygen vacancies that affects tetragonal phase stability [26–31]. Hence, the oxidation state of alloying elements in the oxide film relative to Zr(IV) is expected to have a significant impact. More specifically, any alloying element that is evenly distributed, i.e. a substitutional element in the matrix, and assumes an oxidation states less than (IV) is expected to stabilize the tetragonal phase. Such stabilization has been demonstrated previously through the addition of well-established sub-valent cations to zirconium alloys, such as yttrium [32].

It is expected that the 1–1.2 wt% tin present in Zircaloy-4 and ZIRLO^{TM} occupies substitutional sites in the zirconium and ZrO$_2$ matrices due to the similar metallic and ionic radii of tin and zirconium (2–3 pm difference [33,34]). If a Zr(IV) atom is replaced by a Sn(II) atom, oxygen vacancies must form to balance the charge and ensure electroneutrality of the unit cell; however, if Sn(IV) were present in the lattice, this would not occur. Therefore, if the presence of Sn(II) in the zirconia lattice creates a higher number of oxygen vacancies, it is plausible that it will also act as a stabilising agent for tetragonal zirconia. Recent modelling work [35] and Raman spectroscopy results [36,37] suggest that both Sn(II) and Sn(IV) appear to be present in zirconium alloy oxide films. However,

depth resolved information and quantification of these species has not yet been possible. Further experimental evidence is therefore needed.

In order to provide such evidence, the present work aims at identifying the oxidation state of tin in pre-transition oxide films grown on Zircaloy-4 and ZIRLO^{TM} by means of X-ray absorption near-edge structure (XANES) spectroscopy. This technique has the advantage that it can be applied to the corroded samples without the need for any sample preparation or separation, which might inadvertently affect the sample's tin speciation. To date, XANES and extended X-ray absorption fine structure (EXAFS) have been used to identify the state of elements associated with SPPs in zirconium alloys, such as iron, chromium and niobium [20,38–41]. The present study represents the first identification of the oxidation state of tin in thin zirconium oxide films using XANES. Here, the Sn L$_3$ edge at 3.9 keV was used to assess the oxidation state of tin in thin pre-transition oxide films grown on Zircaloy-4 and ZIRLO^{TM} by comparing edge energies and XANES spectral features to reference specimens (Sn(0) foil, Sn^{II}O and Sn^{IV}O$_2$, as well as Zircaloy-4 and ZIRLO^{TM} metal standard specimens). The incidence angle of the impinging X-rays was varied in the XANES measurement to probe the tin speciation at different depths relative to the sample surface while samples removed after different corrosion duration provided time-resolved information.

2. Materials and methods

2.1. Materials description and oxidation method

Zircaloy-4 (Zr–Sn–Fe–Cr) and ZIRLO^{TM} (Zr–Sn–Nb–Fe) sheet coupons of approximate dimensions 25 mm × 50 mm × 0.5 mm in fully recrystallised condition were corroded in a static isothermal autoclave operating at 360 °C in simulated pressurized water reactor (PWR) primary water chemistry (Li = 2 wt ppm, B = 1000 wt ppm as LiOH and H$_3$BO$_3$). Further details of the autoclave corrosion testing are discussed in [1]. An additional ZIRLO^{TM} sample was corroded in air at 500 °C for 1 h; this corrosion environment was used to obtain a thin (0.5 μm from weight gain) oxide film in a more controlled manner than autoclave corrosion which has longer heating and cooling rates and thus makes production of such a thin oxide film difficult to achieve. The material compositions of these samples are given in Table 1. A list of the samples investigated during this study are provided in Table 2 including the exposure time and oxide thickness (determined from weight gain assuming 1 μm = 15 mg/dm^2 [42]) for each sample. Images from scanning electron microscopy (SEM) support the calculated thicknesses, although the air oxidized sample appeared to contain a 1 μm thick oxide on average measurements from SEM micrographs (Fig. 1). All of the samples studied are within the first cycle of corrosion prior to transition, which is expected to occur when the oxide

Table 1
Chemical composition of alloys characterised in this study.

Alloy	Zr	Fe wt%	Cr wt%	Sn wt%	Nb wt%
Zircaloy-4 sheet	Balance	0.2	0.1	1.2	0.0
ZIRLO^{TM} sheet	Balance	0.1	0.0	0.9	0.9

Table 2
Experimental details of specimens characterised in this study.

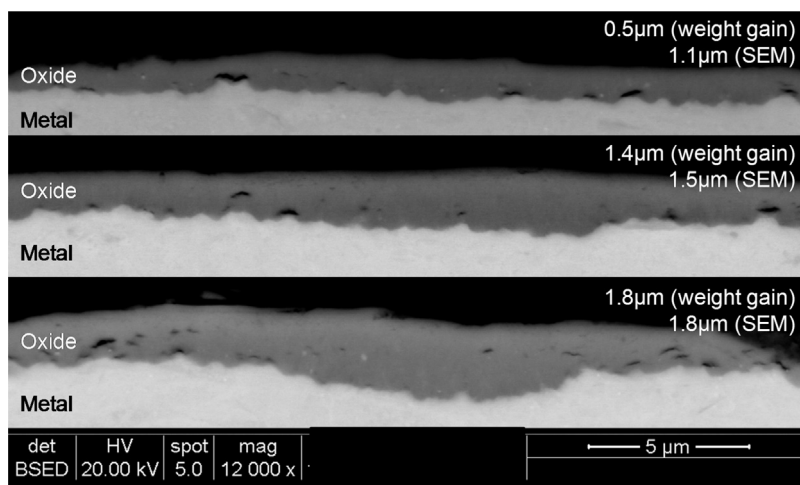| Alloy	Exposure conditions	Exposure time	Oxide thickness from weight gain (μm)
Zircaloy-4	PWR chemistry, 360 °C, 19 MPa	94 days	1.4
ZIRLO^{TM}	PWR chemistry, 360 °C, 19 MPa	94 days	1.8
ZIRLO^{TM}	Air, 500 °C	1 h	0.5

Fig. 1. Micrographs showing the measured oxide thickness from SEM against that predicted from corrosion weight gain measurements.

is approximately 2 μm thick [1]. No additional preparation of the samples was required prior to XANES analysis.

Fresh Zircaloy-4 and ZIRLO[TM] metal coupons, from the same batch of material as the corroded coupons, were used to represent metallic tin standards during the experiment, assuming the tin in these materials is non-oxidised metal. Prior to the investigation, the metal coupons were cleaned using 2400 grit paper to remove any contamination and residual surface oxide and washed with deionized water. A metallic tin foil, and powdered SnO and SnO_2 compounds were also used as references for this experiment, all of which were >97% purity.

2.2. XANES data acquisition

Data was acquired at the I811 beamline at MAX II Laboratory, Lund University, Sweden, using a high photon flux super-conducting multi-pole wiggler beamline [43]. Studies were undertaken at the Sn L_3 edge (3.9 keV), as core–hole lifetime broadening at these lower photoelectron transition energies is much less than at the Sn K edge at 29.2 keV (2.6 eV versus 10.5 eV, respectively) leading to better resolved resonant structures. X-rays from the wiggler were monochromatised using double Si (111) crystals, detuned 70% of the incident intensity to suppress contamination of the beam by higher harmonic wavelengths. A helium sample environment was used to prevent signal loss through air absorption. Data were collected at energies −30 to +90 eV around the Sn L_3 edge using the step sizes listed in Table 3 and a 1 s/step counting time for each data point.

All of the zirconium alloy samples were measured in fluorescence mode at an angle between 12°–45° relative to the photon beam to alter the penetration depth of the incoming beam. The samples were rotated 90° normal to the beam direction in order to ensure that observed XANES differences were not due to a preferred orientation of crystallites and therefore associated with differences in X-ray penetration depth. Four scans at each angle were acquired and merged together during data processing to improve the signal-to-noise ratio. The pure tin compounds were measured in transmission mode using a helium filled ionization chamber, col-

lecting three scans each for data processing. A Sn L_3 XANES of the tin foil was recorded between each storage ring injection (every 12 h) and the first inflection of the spectrum was used to calibrate the monochromator energy (3.9 keV).

Data were analyzed using the Athena code, part of the Demeter software package [44].

2.3. Calculations of penetration depth

The penetration depth was calculated for an energy of 3.9 keV, assuming the oxide formed is monoclinic ZrO_2 with a density of 5.84 g/cm^3. Using the mass attenuation coefficients for Zr and O (851 cm^2/g and 93.2 cm^2/g respectively for an energy of 4 keV, [45]) in Eq. (1), the mass attenuation coefficient for ZrO_2 is determined to be 653 cm^2/g.

$$\frac{\mu}{\rho} = \sum_i w_i \left(\frac{\mu}{\rho}\right)_i = \frac{92}{124}\left(\frac{\mu}{\rho}\right)_{Zr} + \frac{32}{124}\left(\frac{\mu}{\rho}\right)_O \qquad (1)$$

where w_i is the weight fraction of species i, μ is the mass attenuation coefficient and ρ is the density. The attenuation length (x) required for the photon beam intensity to drop to 1/e of its initial intensity, I_0, can be obtained using Eq. (2).

$$\frac{I}{I_0} = \frac{1}{e} = \exp(-\mu x) \qquad (2)$$

The attenuation length, x, is therefore equal to $1/\mu$, calculated as 2.48 μm for an energy of 3.9 keV (assuming monoclinic ZrO_2). The oxide depth probed by the X-ray beam at different incident angles, θ (Fig. 2), can then be calculated using basic trigonometry; these are listed in Table 4.
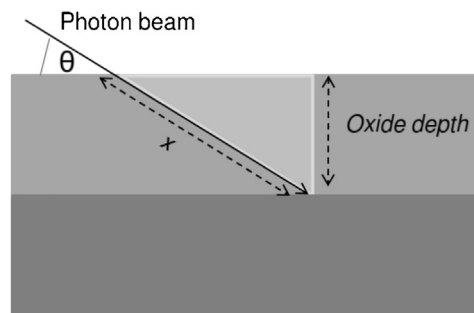

Fig. 2. Schematic indicating Photon beam incidence angle (θ) and penetration depth (x) for calculating the oxide depth analysed by XANES.

Table 3
Experimental conditions for data collection.

Energy range around L_3 edge (eV)	Step size (eV)
−30 to −10	1 eV
−10 to +50	0.3 eV
50 to +90	1 eV

Table 4
X-ray beam incident angle, θ, beam attenuation length, x, and associated oxide penetration depth probed.

Angle (°)	Oxide probe depth (μm)
12	0.5
30	1.3
45	1.8

3. Results

3.1. Comparison of oxide films with standard compounds

Fig. 3 compares the Sn L$_3$ edge spectra of the Zircaloy-4 metal, the Zircaloy-4 oxide and the reference spectra (i.e. Sn, SnO, SnO$_2$). A clear difference between the Zircaloy-4 metal and the Zircaloy-4 oxide spectra is observed, indicating tin is in a different chemical environment when the oxide film is formed. The onset of the rising absorption edge is at a lower energy for the Zircaloy-4 metal compared to the Zircaloy-4 oxide. Furthermore, the Zircaloy-4 oxide spectra resonant features are different than the Sn, SnO and SnO$_2$ reference spectra. It is well established that the 1–1.2 wt% tin in the alloys studied occupies substitutional sites in the zirconium and zirconia matrices due to the similar metallic and ionic radii of tin and zirconium [33,34]. Therefore, the structural environment of tin in zirconium alloys and oxide layers will be significantly different to that for pure tin and in bulk tin oxides. This explains the spectral differences between samples and references observed. Note that the oxidised layer has a Sn L$_3$ XANES signature that is similar to the 'amorphous' SnO$_2$ reported in Jiménez et al. [46]. which contained a mixture of amorphous SnO$_2$ nanoparticles, SnO and Sn(0).

Comparison of Zircaloy-4 and ZIRLO^{TM} metal XANES spectra in Fig. 4 reveals no significant differences between them. The spectra recorded for the oxide films for these two alloys, grown to similar thickness (Fig. 5a and Fig. 6a, respectively) also appear similar. We may therefore conclude that the speciation or chemical and structural environment of tin is similar in both alloys and their corroded oxide layers despite the different alloying elements of Nb (ZIRLO^{TM}) and Cr (Zircaloy-4) present in these alloys.

While the metallic tin XANES is relatively featureless in the region of the rising edge, the SnO and SnO$_2$ XANES exhibit sharp features, which are more more pronounced for the latter. Both also have a defined maximum absorption peak, but at different energy positions, 3953 eV and 3960 eV for SnO and SnO$_2$ respectively (Table 5). Similar features are also observed for the zirconium alloy materials but with a slightly shifted energy. This indicates a different local environment of tin in each of these alloys. Additionally, subtle features in the near edge region (beyond 3960 eV) are also different, which would not be the case if tin was in an environment identical to that in the metallic and oxide compounds.

3.2. Depth profiling results

Fig. 5a shows XANES spectra for different penetration depths of the oxide film formed on Zircaloy-4, i.e. by varying θ. The resonant features (pre-edge at ~3930 eV, feature on the rising edge at ~3944 eV and the main absorption maximum at ~3956 eV) in all spectra appear similar, indicating that tin is in a similar coordination environment throughout the oxide film thickness. However, there appears to be a shift in the edge position to higher energy for spectra recorded at a shallow incident angle such that the X-rays penetrate only the outer part of the oxide film.

This observed shift in the edge position was quantified by comparison to the oxidation state of tin in the pure tin metal and oxide reference compounds. The results are shown in Fig. 5b, where the tin oxidation state energy is plotted as a function of ionisation
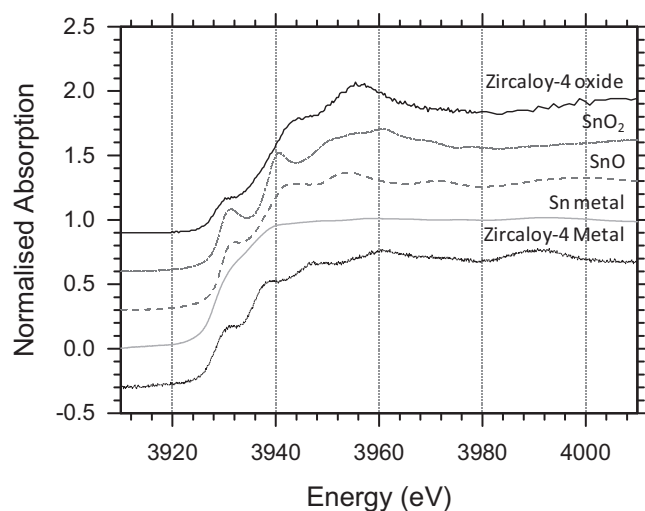

Fig. 3. Sn L$_3$ edge XANES spectra of tin standards (Sn^0, Sn^{II}O, Sn^{IV}O$_2$), Zircaloy-4 oxide (1.4 μm, measured at an incidence angle of 30°) and Zircaloy-4 metal. Spectra are shifted on the y-axis for clarity.
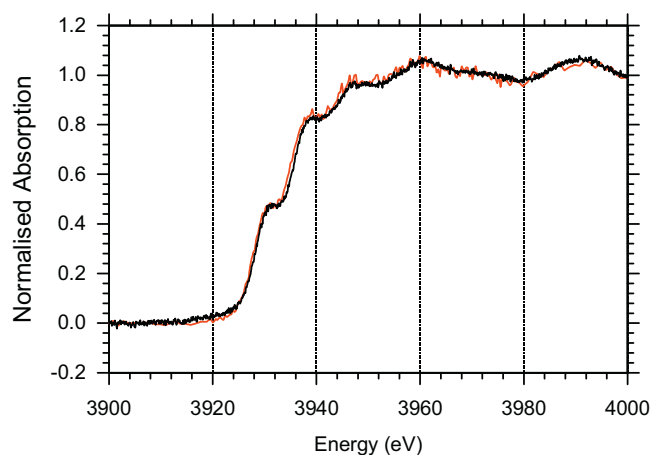

Fig. 4. Sn L$_3$ edge XANES spectra of Zircaloy-4 (black) and ZIRLO^{TM} (red) metals. (For interpretation of the references to colour in this figure legend, the reader is referred to the web version of this article.).

Table 5
Energy of the first three features observed in the edge and near-edge region of Zircaloy-4 metal and oxide films and reference spectra (SnO, SnO$_2$).

Material	Energy (eV)		
	Feature 1	Feature 2	Feature 3
Zircaloy-4 metal	3931.17	3938.42	3946.79
Zircaloy-4 oxide (1.4 μm)	3930.64	3944.20	3956.04
SnO	3931.08	3941.96	3953.63
SnO$_2$	3931.25	3940.28	3960.70

energy, E_0. The value of E_0 in each spectra was defined as the energy at half the normalised height of the edge. The trend of increasing E_0 with increasing tin oxidation state for the Sn^0, Sn^{II}O, Sn^{IV}O$_2$ reference spectra is determined via linear regression and is seen plotted as a straight line in Fig. 5b. The ionisation energy measured for tin in the Zircaloy-4 metal, assumed to be Sn(0), is shifted about 4 eV to higher energy compared to the tin metal foil. This is likely because of the unique coordination environment of tin in Zircaloy-4, which is known to sit in substitutional zirconium lattice sites in the metal alloy with hexagonal close-packed structure instead of rhombohedral for Sn(0) [34]. The ionisation energy values for XANES probed at different depths of the Zircaloy-4 oxide layer are plotted along
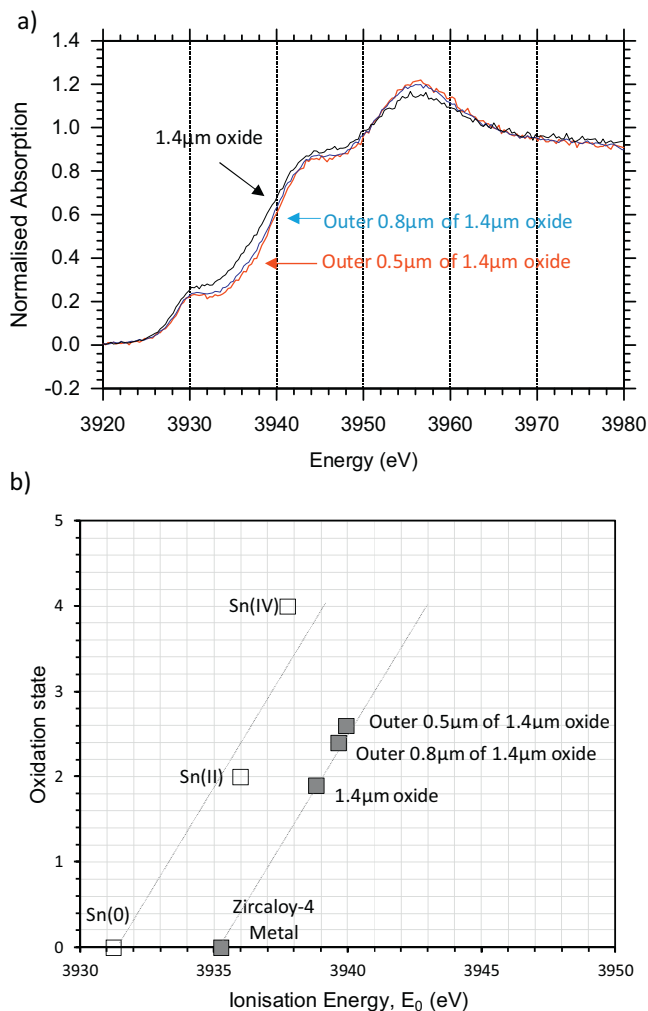
a)

a)

b)

b)

Fig. 5. a) Sn L$_3$ XANES spectra recorded at varying θ to probe different depths of a 1.4 μm oxide film formed on Zircaloy-4 and b) E_0 positions for the spectra obtained at different oxide depths (closed symbols) with those for the Sn references (open symbols).

Fig. 6. a) Sn L$_3$ XANES spectra for a 1.8 μm oxide film formed on ZIRLO^{TM} probed at two different depths, compared to a 0.5 μm oxide film ZIRLO^{TM} sample; b) E_0 positions for the spectra obtained at different oxide depths (closed symbols) with those for the Sn references (open symbols).

the same trend as the reference, but shifted on the x-intercept to account for the observed shift between Zircaloy-4 metal and the Sn(0) foil. The result indicates that the oxide layer likely contains Sn(II) and Sn(IV) and that the average oxidation state of the outermost Zircaloy-4 oxide layer contains the highest amount of Sn(IV).

Fig. 6 depicts the Sn L$_3$ XANES and ionisation energies recorded for different depths (i.e. incident angles or distances within the metal/oxide interface) of ZIRLO^{TM} oxides. The measurements in this case included an additional sample with an oxide thickness of 0.5 μm from weight gain. This allows two comparisons to be made:

1. The tin is in a higher oxidation state (on average) in the outer 0.5 μm of the ZIRLO^{TM} sample compared to the average across the entire oxide thickness (1.8 μm). These results are consistent with findings from Zircaloy-4 oxide.
2. Comparing the thin 0.5 μm film with the outer 0.5 μm of a thicker oxide film (bearing in mind zirconium corrosion occurs at the metal/oxide interface, whereby new oxide is formed [47,48]) shows the gradual oxidation of tin from a lower oxidation state in the thin film (new oxide) to higher in the outer (aged) oxide. This supports the gradual oxidation of tin, which is slower than zirconium.
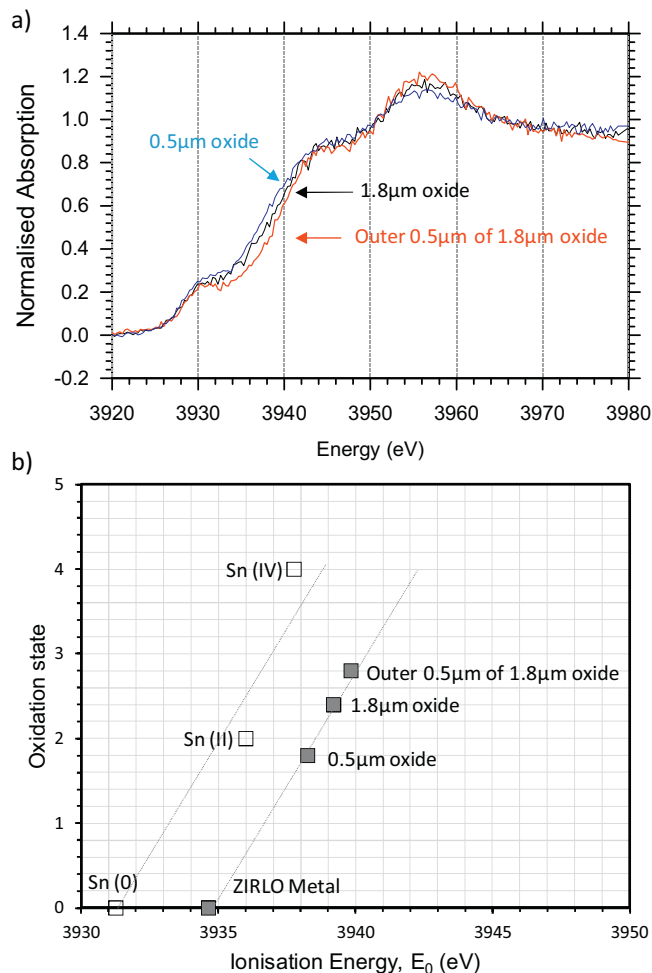
Similar to Zircaloy-4, the spectra and the ionisation energy position plots for ZIRLO^{TM} clearly show a shift to higher E_0 with decreasing penetration depth of the photon beam. Hence, measurements of both alloys indicate the outer oxide contains tin in a higher oxidation state than the average oxidation state of the entire oxide. The 0.5 μm thick sample shows the lowest E_0 value of the oxide layer measurements indicating newly formed oxide has a lower average oxidation state, assumed to be due to the formation of Sn(II) on initial incorporation of Sn(0) from the metal into the oxide film.

4. Discussion

The authors observed that the Sn L$_3$ E_0 position shifts to higher energy when using a shallower glancing angle to probe the oxide film, i.e. when only the outer part of the oxidised film is probed, compared to the entire oxide thickness. Zirconium oxidation proceeds via inward diffusion of oxygen ion forming fresh oxide at the metal/oxide interface [47,48]. This indicates that the outer 'aged' oxide layer has a higher average oxidation state than newly formed oxide adjacent to the metal/oxide interface. Our results show that tin in the Zircaloy-4 and ZIRLO^{TM} oxides has an average oxidation state between Sn(II) and Sn(IV), with the average oxidation state lowest for measurements probing the entire oxide film, i.e. including data from near the metal/oxide interface, and highest when

probing only the outer 0.5 μm of oxide. The positive shift in E_0 from entire oxide film to outer-layer indicates a decrease in the Sn(II)/Sn(IV) ratio with oxide growth.

The authors interpret these results as an indication that Sn(0) in the metal first tends to oxidise to Sn(II) in the newly formed oxide film. As the oxide forms, subsequent inward displacement of the metal/oxide interface occurs with continued oxide layer growth. As the interface continues to move inwards and the oxide layer thickens, Sn(II) becomes oxidised to a higher Sn(IV) oxidation state as it moves further from the metal/oxide interface. This is supported by the observation that the Sn(II)/Sn(IV) ratio is higher in a thin 0.5 μm thick oxide than the outer 0.5 μm of thicker oxide sample (>1.4 μm). In other words, our observed trend of increasing Sn L_3 E_0 energies with increasing probed Zircaloy-4 and ZIRLO^{TM} oxide layer depth indicate oxidation from Sn(0) (metal), to Sn(II) (newly formed oxide), to Sn(IV) ('aged' oxide).

The relevance of these findings is important for the wider research community in relation to the degradation of the protective nature of the oxide film, which is thought to be responsible for the enhanced corrosion kinetics observed in the presence of tin. The presence of Sn(II) will affect the number of oxygen vacancies in the ZrO$_2$ matrix and is likely to assist in stabilising tetragonal ZrO$_2$. The presence of oxygen vacancies might also assist transport of oxygen ions through the oxide film [49] if oxygen diffusion is the rate limiting step for zirconium corrosion as reported in [50,51]. Further, when Sn(II) oxidises to Sn(IV) it will loose its ability to stabilise tetragonal ZrO$_2$ and therefore will transform to monoclinic ZrO$_2$. This is an important point since the tetragonal to monoclinic phase transformation in thin ZrO$_2$ films has been previously associated with a reduction of compressive stresses in the ageing oxide as the metal/oxide interface moves inwards [7,52,53]. It is this phase transformation that is likely to result in crack formation in the oxide film due to the associated transformation strain and change in volume of oxide. While a significant stress gradient in microns thick oxide films is difficult to justify, the further oxidation of Sn(II) to Sn(IV) relatively near the metal/oxide interface provides a good reason for the early tetragonal to monoclinic phase transformation as observed in [7]. Again, these cracks may create pathways to allow oxidising media to advance closer to the metal/oxide interface, reducing the diffusion pathway for oxygen ion diffusion.

Due to the angles used and the undulating interface formed during zirconium alloy corrosion, it is possible that some tin from the underlying metal could contribute to the fluorescence signal in these measurements. However, any contribution from the metal is likely to be small, as the θ angles used were selected to probe just the entire oxide thickness in an attempt to eliminate signal from the underlying metal. Our results corroborate suggested mechanisms discussed in the literature from modelling studies [35], which propose that Sn(II) initially forms at the metal/oxide interface when tin is incorporated into the newly formed oxide film.

Attempts were undertaken to quantify the phase fractions of Sn(II) and Sn(IV) in the oxide film, initially via a linear combination fitting procedure using the tin standards. As the Sn L_3 XANES of the oxidised layers were similar to the mixture of amorphous SnO$_2$ nanoparticles, Sn(0) and SnO reported in [46], the authors thought this was promising. However, such a simple fitting procedure was not successful and more complex simulations are required. While tin is often referred to as sitting uniformly in the zirconium matrix, recent atom probe tomography [25] has shown tin appears uniformly across most parts of the oxide thickness but also forms cluster species, which are observed to form randomly at isolated locations within the oxide film. Thus successful fits to the data for tin in the oxide film will likely require better matched reference spectra, including XANES for both isolated tin atoms in the (distorted) zirconium oxide lattice of varying oxidation state and tin in multi-nuclear tin clusters.

5. Conclusions

This paper describes the first use of XANES to characterise the oxidation state of alloying additions of tin (1–1.2 wt%) in thin oxide layers formed on nuclear grade zirconium alloys. The main conclusions drawn from this work are:

1. The chemical environment of tin in oxide films formed on ZIRLO^{TM} and Zircaloy-4 is similar, despite the addition of Nb in ZIRLO^{TM} and Cr in Zircaloy-4.
2. The chemical environment of tin in the oxide layer is different to that in the pure tin metal and in the zirconium alloy metal.
3. Depth resolved spectra indicate the average oxidation state of tin at the metal/oxide interface is lower than in the outer 0.5 μm of oxide, suggesting a gradual oxidation process as the oxide layer thickens.
4. The above is further confirmed by the lower average tin oxidation state for a freshly formed 0.5 μm oxide film compared to that in the outer 0.5 μm of a thicker 1.8 μm oxide.
5. Comparing E_0 values for the different measurements indicates tin may be initially oxidised to Sn(II) and then becomes oxidised to Sn(IV) as the oxide layer grows thicker and the tin in the outer oxide is aged. This is in agreement with literature modelling data and may contribute to tin's ability to stabilise tetragonal oxide phase near the metal/oxide interface.

References

[1] J. Wei, P. Frankel, M. Blat, A. Ambard, R.J. Comstock, L. Hallstadius, S. Lyon, R.A. Cottis, M. Preuss, Autoclave study of zirconium alloys with and without hydride rim, Corros. Eng. Sci. Technol. 7 (2012) 516–528.
[2] E. Hillner, D.G. Franklin, J.D. Smee, Long term corrosion of Zircaloy before and after irradiation, J. Nucl. Mater. 278 (2000) 334–345.
[3] R. Adamson, F. Garzarolli, B. Cox, A. Strasser, P. Rudling, Corrosion Mechanisms in Zirconium Alloys, ZIRAT12/IZNA7 Special Topics Report, ANT International Sweden (2007).
[4] B. Cox, Some thoughts on the mechanisms of in-reactor corrosion of zirconium alloys, J. Nucl. Mater. 336 (2005) 331–368.
[5] M. Harada, R. Wakamatsu, The Effect of Hydrogen on the Transition Behaviour of the Corrosion Rate of Zirconium Alloys, Zirconium in the Nuclear Industry: 15th International Symposium, Sunriver, Oregon, ASTM STP 1505 (2009) 384–404.
[6] K. Baur, F. Garzarolli, H. Ruhmann, H.J. Sell, Electrochemical Examinations in 350 °C Water with respect to the Mechanism of Corrosion-Hydrogen Pickup, Zirconium in the Nuclear Industry: 12th International Symposium Toronto, Canada, ASTM STP 1354 (2000) 836–852.
[7] J. Wei, P. Frankel, M. Blat, A. Ambard, R.J. Comstock, L. Hallstadius, D. Hudson, G.D.W. Smith, C.R.M. Grovenor, M. Klaus, R.A. Cottis, S. Lyon, M. Preuss, The effect of Sn on autoclave corrosion performance and corrosion mechanisms in Zr–Sn–Nb alloys, Acta Mater. 61 (2013) 4200–4214.
[8] R.C. Garvie, The occurrence of metastable tetragonal zirconia as a crystallite size effect, J. Phys. Chem. 69 (1965) 1238–1243.
[9] A.J.G. Maroto, R. Bordoni, M. Villegas, A.M. Olmedo, M.A. Blesa, A. Iglesias, P. Koenig, Growth and characterisation of oxide layers on zirconium alloys, J. Nucl. Mater. 229 (1996) 79–92.
[10] T. Arima, T. Masuzumi, H. Furuya, K. Idemitsu, Y. Inagaki, The oxidation kinetics and the structure of the oxide film on Zircaloy before and after the kinetic transition, J. Nucl. Mater. 294 (2001) 148–153.

[11] W. Qin, C. Nam, H.L. Li, J.A. Szpunar, Effects of local stress on the stability of tetragonal phase in ZrO2, J. Alloys. Comp. 437 (1,2) (2007) 280–284.

[12] A. Garner, A. Gholinia, P. Frankel, M. Gass, I. MacLaren, M. Preuss, The microstructure and microtexture of zirconium oxide films studied by t-EBSD and automated crystal orientation mapping with TEM, Acta Mater. 80 (2014) 159–171.

[13] J. Godlewski, P., Bouvier, G., Lucazeau, L. Fayette, Stress Distribution Measured by Raman Spectroscopy in zirconia Films Formed by Oxidation of Zr-Based Alloys, Zirconium in the Nuclear Industry: 12th International Symposium, Toronto, Canada, ASTM STP 1354 (2000) 877–899.

[14] W. Gong, H. Zhang, Y. Qiao, H. Tian, X. Ni, Z. Li, X. Wang, Grain morphology and crystal structure of pre-transition oxides formed on Zircaloy-4, Corros. Sci. 74 (2013) 323–331.

[15] A. Yilmazbayhan, A.T. Motta, R.J. Comstock, G.P. Sabol, B. Lai, Z. Cai, Structure of zirconium alloy oxides formed in pure water studied with synchrotron radiation and optical microscopy: relation to corrosion rate, J. Nucl. Mater. 324 (2004) 6–22.

[16] W. Qin, C. Nam, H.L. Li, J.A. Szpunar, Tetragonal phase stability in ZrO2 film formed on zirconium alloys and its effects on corrosion resistance, Acta Mater. 55 (2007) 1695–1701.

[17] B. Cox, Processes occurring during the breakdown of oxide films on zirconium alloys, J. Nucl. Mater. 29 (1969) 50–66.

[18] T. Isobe, Y. Matsuo, Development of Highly Corrosion Resistant Zirconium-Base Alloys, Zirconium in the Nuclear Industry: 9th International Symposium, Kobe, Japan, ASTM STP 1132 (1991) 346–367.

[19] G. Sundell, M. Thuvander, H.-O. Andren, Barrier oxide chemistry and hydrogen pick-up mechanisms in zirconium alloys, Corros. Sci. 102 (2016) 490–502.

[20] A. Couet, A.T. Motta, A. Ambard, The coupled current charge compensation model for zirconium alloy fuel cladding oxidation: I. Parabolic oxidation of zirconium alloys, Corros. Sci. 100 (2015) 73–84.

[21] A. Couet, A.T. Motta, R.J. Comstock, Hydrogen pick-up measurements in zirconium alloys: relation to oxidation kinetics, J. Nucl. Mater. 451 (2014) 1–13.

[22] J. Schefold, D. Lincot, A. Ambard, O. Kerrec, The cyclic nature of corrosion of Zr and Zr–Sn in high temperature water (633 K), J. Electro. Soc. 10 (2003) B451–B461.

[23] K. Takeda, H. Anada, Mechanism of Corrosion Rate Degradation Due to Tin, Zirconium in the Nuclear Industry: 12th International Symposium, Toronto, Canada, ASTM STP 1354 (2000) 592–607.

[24] P. Barberis, A. Frichet, Characterisation of Zircaloy-4 oxide layers by impedance spectroscopy, J. Nucl. Mater. 273 (1999) 182–191.

[25] G. Sundell, M. Thuvander, H.-O. Andrén, Tin clustering and precipitation in the oxide during autoclave corrosion of Zircaloy-2, J. Nucl. Mater. 456 (2015) 409–414.

[26] P. Aldebert, J.-P. Traverse, Structure and ionic mobility of zirconia at high temperatures, J. Am. Ceram. Soc. 1 (1985) 34–40.

[27] G. Stefanic, S. Musić, Factors influencing the stability of low temperature tetragonal ZrO2, Croat. Chem. Acta 3 (2002) 727–767.

[28] X. Guo, Property degradation of tetragonal zirconia induced by low-temperature defect reaction with water molecules, Chem. Mater. 21 (2004) 3988–3994.

[29] M. Youseff, B. Yildiz, Intrinsic point-defect equilibria in tetragonal ZrO2: density functional theory analysis with finite-temperature effects, Phys. Rev. B 14 (2012), 144109.

[30] M.J. Torralvo, M.A. Alario, J. Soria, Crystalisation behaviour of zirconium oxide gels, J. Catal. 86 (1984) 473–476.

[31] M.I. Osendi, J.S. Moya, C.J. Serna, J. Soria, Metastability of tetragonal zirconia powders, J. Am. Ceram. Soc. 68 (3) (1985) 135–139.

[32] W. Gong, H. Zhang, C. Wu, H. Tian, X. Wang, The role of alloying elements in the initiation of nanoscale porosity in oxide films formed on zirconium alloys, Corros. Sci. 77 (2013) 391–396.

[33] R.D. Shannon, C.T. Prewitt, Effective ionic radii in oxides and fluorides, Acta Crystallogr. B 25 (1969) 925–946.

[34] A.F. Wells, Structural Inorganic Chemistry, 5th ed., Clarendon Press, Oxford, 1984.

[35] B.D.C. Bell, S.T. Murphy, P.A. Burr, R.W. Grimes, M.R. Wenman, Accommodation of tin in tetragonal ZrO2, J. Appl. Phys. 117 (8) (2015), 084901.

[36] D. Pêcheur, V.P., Filippov, A.B. Bateev, J.J. Ivanov, Mössbauer investigations of the chemical states of tin and iron atoms in zirconium alloy oxide films Zirconium in the Nuclear Industry: 13th International Symposium, Annecy, France, ASTM STP 1423 (2002) 135–152.

[37] H. Anada, K., Takeda, S., Nasu, Y., Kobayashi, T. Nakamichi, Chemical State Analysis of Sn and Fe in ZrO2 by Mössbauer Spectroscopy, Zirconium in the Nuclear Industry: 13th International Symposium, Annecy, France, ASTM STP 1423 (2002) 154–168.

[38] A. Froideval, C. Degueldre, C.U. Segre, M.A. Pouchon, D. Grolimund, Niobium speciation at the metal/oxide interface of corroded niobium-doped Zircaloys: a X-ray absorption near-edge structure study, Corros. Sci. 50 (2008) 1313–1320.

[39] K. Sakamoto, K. Une, M. Aomi, K. Hashizume, Depth profile of chemical states of alloying elements in oxide layer of Zr-based alloys, Prog. Nucl. Energy 57 (2012) 101–105.

[40] G. Kuri, C. Degueldre, J. Bertsch, S. Abolhassani, Micro-focussed XAFS spectroscopy to study Ni-bearing precipitates in the metal of corroded Zircaloy-2, Appl. Phys. A: Mater. Sci. Process 98 (2010) 625–633.

[41] A. Couet, A.T. Motta, B. De Gabory, Z. Cai, Microbeam X-ray absorption near-edge spectroscopy study of the oxidation of Fe and Nb in zirconium alloy oxide layers, J. Nucl. Mater. 452 (2014) 614–627.

[42] A.T. Motta, A. Yilmazbayhan, R.J. Comstock, S.G.P. Partezana, B. Lai, Microstructure and growth mechanism of oxide layers formed in Zr Alloys studied with micro beam synchrotron radiation, J. ASTM Int. 2 (2005), Paper # JAI 12375.

[43] S. Carlsson, M. Clausen, L. Gridneva, B. Sommarin, C. Svensson, XAFS experiments at beamline I811, MAX-lab synchrotron source, Sweden, J. Synchrotron. Radiat. 13 (2006) 359–364.

[44] B. Ravel, M. Newville, ATHENA, ARTEMIS. HEPHAESTUS: data analysis for X-ray absorption spectroscopy using IFEFFIT, J. Synchrotron. Radiat. 12 (2005) 537–541.

[45] http://physics.nist.gov/PhysRefData/XrayMassCoef/chap2.html.

[46] V.M. Jiménez, A. Caballero, A. Fernandez, J.P. Espinós, M. Ocana, A.R. González-Elipe, Structural characterisation of partially amorphous SnO2 nanoparticles by factor analysis of XAS and FT-IR spectra, Solid State Ionics 116 (1999) 117–127.

[47] B. Cox, J.P. Pemsler, Diffusion of oxygen in growing zirconia films, J. Nucl. Mater. 28 (1968) 73.

[48] S.S. Yardley, K.L. Moore, N. Ni, J.F. Wei, S. Lyon, M. Preuss, S. Lozano-Perez, C.R.M. Grovernor, An investigation of the oxidation behaviour of zirconium alloys using isotopic tracers and high resolution SIMS, J. Nucl. Mater. 443 (2013) 436–443.

[49] M. Lindgren, I. Panas, On the fate of hydrogen during zirconium oxidation by water; effect of oxygen dissolution in alpha-Zr, RSC Adv. 4 (2014) 11050–11058.

[50] M.M.R. Howlader, K. Shiiyama, C. Kinoshita, M. Kutsuwada, M. Inagaki, The electrical conductivity of Zircaloy oxide films, J. Nucl. Mater. 253 (1998) 149–155.

[51] M. Tupin, M. Pijolat, F. Valdivieso, M. Soustelle, A. Frichet, P. Barberis, Differences in reactivity of oxide growth during the oxidation of Zircaloy-4 in water vapour before and after the kinetic transition, J. Nucl. Mater. 317 (2003) 130–144.

[52] M. Preuss, P. Frankel, S. Lozano-Perez, D. Hudson, E. Polatidis, N. Ni, J. Wei, C. English, S. Storer, K.B. Chong, M. Fitzpatrick, P. Wang, J. Smith, C. Grovenor, G. Smith, J. Sykes, B. Cottis, S. Lyon, L. Hallstadius, R.J. Comstock, A. Ambard, M. Blat-Yrieix, Studies regarding corrosion mechanisms in zirconium alloys, Zirconium in the Nuclear Industry: 16th International Symposium, ASTM STP 1529, (2011) 649–681.

[53] P. Frankel, J. Wei, E.M. Francis, A. Forsey, N. Ni, S. Lozano-Perez, A. Ambard, M. Blat-Yriex, R.J. Comstock, L. Hallstadius, R. Moat, C.R.M. Grovenor, S. Lyon, R.A. Cottis, M. Preuss, Effect of Sn on corrosion mechanisms in advanced Zr-cladding for pressurised water reactors, Zirconium in the Nuclear Industry: 17th International Symposium, ASTM STP 1543, (2015) 404–433.